bioRxiv preprint doi: https://doi.org/10.1101/2020.12.12.422444; this version posted December 12, 2020. The copyright holder for this preprint (which was not certified by peer review) is the author/funder, who has granted bioRxiv a license to display the preprint in perpetuity. It is made available under aCC-BY 4.0 International license.

Choice of fluorophore affects dynamic DNA nanostructures

Kevin Jahnke,[†,‡] Helmut Grubmüller,[¶] Maxim Igaev,[*,¶] and Kerstin Göpfrich[*,†,‡]

†*Max Planck Institute for Medical Research, Biophysical Engineering Group, Jahnstraße 29, 69120 Heidelberg, Germany*

1

‡*Department of Physics and Astronomy, Heidelberg University, 69120 Heidelberg, Germany*

¶*Max Planck Institute for Biophysical Chemistry, Department of Theoretical and Computational Biophysics, Am Fassberg 11, 37077 Göttingen, Germany*

E-mail: maxim.igaev@mpibpc.mpg.de; kerstin.goepfrich@mr.mpg.de

bioRxiv preprint doi: https://doi.org/10.1101/2020.12.12.422444; this version posted December 12, 2020. The copyright holder for this preprint (which was not certified by peer review) is the author/funder, who has granted bioRxiv a license to display the preprint in perpetuity. It is made available under aCC-BY 4.0 International license.

Abstract

The ability to dynamically remodel DNA origami structures or functional nanodevices is highly desired in the field of DNA nanotechnology. Concomitantly, the use of fluorophores to track and validate the dynamics of such DNA-based architectures is commonplace and often unavoidable. It is therefore crucial to be aware of the side effects of popular fluorophores, which are often exchanged without considering the potential impact on the system. Here, we show that the choice of fluorophore can strongly affect the reconfiguration of DNA nanostructures. To this end, we encapsulate a triple-stranded DNA (tsDNA) into water-in-oil compartments and functionalize their periphery with a single-stranded DNA handle (ssDNA). Thus, the tsDNA can bind and unbind from the periphery by reversible opening of the triplex and subsequent strand displacement. Using a combination of experiments, molecular dynamics (MD) simulations, and reaction-diffusion modeling, we demonstrate for twelve different fluorophore combinations that it is possible to alter or even inhibit the DNA nanostructure formation – without changing the DNA sequence. Besides its immediate importance for the design of pH-responsive switches and fluorophore labelling, our work presents a strategy to precisely tune the energy landscape of dynamic DNA nanodevices.

Introduction

DNA nanotechnology has been highly successful in repurposing the iconic DNA double helix to create programmable molecular architectures. Once focused on static shapes, dynamic and stimuli-responsive DNA nanoscale devices are gaining a large surge of interest for various applications[1] – from sensors,[2–4] biocomputing algorithms,[5] and drug delivery systems[6,7] to programmable robotic modules[8,9] and functional components for synthetic cells.[10–12] In a vast majority of such reconfigurable systems, dynamics is achieved using strand displacement reactions,[13,14] flexible single-stranded hinges,[15] or stimuli-responsible DNA modifications[16,17] and sequence motifs.[4,18] The ability to reversibly actuate artificial

bioRxiv preprint doi: https://doi.org/10.1101/2020.12.12.422444; this version posted December 12, 2020. The copyright holder for this preprint (which was not certified by peer review) is the author/funder, who has granted bioRxiv a license to display the preprint in perpetuity. It is made available under aCC-BY 4.0 International license.

structures at the nanoscale is therefore at the core of dynamic DNA nanotechnology. Direct measurements of conformational changes in aqueous solutions are often conducted with Förster resonance energy transfer (FRET) or fluorescence microscopy.[19–21] These methods can provide a readout of the overall conformational state of the structure, for example, open *versus* closed, or bound *versus* unbound. Hence, the use of fluorescent dyes is commonplace to validate and quantify the functionality of the DNA-based devices. Fluorophore-tagged DNA nanostructures have also been used as nanoscopic rulers for fluorescence microscopy[22] and to enable the acquisition of super-resolution images with DNA-PAINT.[23] Factors like solubility, photostability and excitation/emission spectra usually play the decisive role in choosing the suitable dye, while potential side effects on the DNA conformation such as overstabilization of DNA duplexes[24] or specific fluorophore-DNA interactions[25] are not the main concern.

Here, we show that the choice of the fluorophore itself can alter the equilibrium conformation and even inhibit a desired dynamic response. We use a pH-responsive triple-stranded DNA motif (tsDNA) combined with a strand-displacement reaction to exemplify that the dynamics can be strongly influenced by the choice of the fluorophore. With all-atom molecular dynamics (MD) simulations, we show that fluorophore-dependent conformational dynamics of the single-stranded DNA (ssDNA) contributes to this observation. By releasing caged protons inside droplet-based confinement, we find that also the duplex dissociation is affected by the fluorophore. Using a reaction-diffusion model, we derive the apparent dissociation constant for 12 different experimentally tested fluorophore combinations. A profound knowledge about the effect that fluorophores and other chemical modifications have on the dynamics of a DNA-based system can be leveraged to realize the desired functionality.

bioRxiv preprint doi: https://doi.org/10.1101/2020.12.12.422444; this version posted December 12, 2020. The copyright holder for this preprint (which was not certified by peer review) is the author/funder, who has granted bioRxiv a license to display the preprint in perpetuity. It is made available under aCC-BY 4.0 International license.

52 # Materials and Methods

53 ## DNA sequence design

54 The DNA sequences were adapted from Green et al.[4] To enable self-assembly at the
55 droplet-periphery, the ssDNA (termed 'Regulator' in Green et al.) was modified with
56 a cholesterol-tag (sequence: 5' Cy3/Alexa488/Cy5/-ACCAGACAATACCACACAATTTT-
57 CholTEG 3', HPLC purified). The tsDNA (termed 'Sensor' in Green et al.) contained
58 the triple-stranded DNA motif as well as a stem loop complementary to the ssDNA. A
59 fluorophore modification was added to its 5' end (sequence: 5' Cy5/Cy3/Atto488/Atto647-
60 TTCTCTTCTCGTTTGCTCTTCTCTTGTGTGGTATTGTCTAAGAGAAGAG 3', HPLC
61 purified). Both DNA sequences were purchased from Biomers or Integrated DNA Technolo-
62 gies and dissolved in ultrapure water (Milli-Q) to exclude the impact of DNA storage buffer
63 on the pH.

64 ## Formation of DNA-containing water-in-oil droplets

65 For the formation of water-in-oil droplets, the DNA-containing aqueous phase was layered
66 on top of the oil phase in a volumetric ratio of 1:3 within a microtube (Eppendorf). Droplet
67 formation was induced by manual shaking for about 4 s as described earlier.[26] For the oil-
68 phase, 1.4 vol% of perflouro-polyether-polyethylene glycol (PFPE-PEG) block-copolymer
69 fluorosurfactants (008-PEG-based fluorosurfactant, Ran Biotechnologies, Inc.) dissolved in
70 HFE-7500 oil (DuPont) was used. The interfacially active surfactants stabilize the droplets.
71 The aqueous phase was composed of 10 mM $MgCl_2$ and 250 mM potassium phosphate buffer
72 adjusted to pH values from 4.3 to 8.0. Cholesterol-tagged ssDNA and the tsDNA were added
73 to the aqueous phase at concentrations of 1.66 µM and 1.25 µM, respectively, if not stated
74 otherwise. ssDNA was added in excess to ensure that there are sufficient binding sites for the
75 tsDNA. Other contents were encapsulated by adding them to the aqueous phase as described
76 in text.

bioRxiv preprint doi: https://doi.org/10.1101/2020.12.12.422444; this version posted December 12, 2020. The copyright holder for this preprint (which was not certified by peer review) is the author/funder, who has granted bioRxiv a license to display the preprint in perpetuity. It is made available under aCC-BY 4.0 International license.

Confocal fluorescence microscopy

For confocal microscopy, the DNA-containing droplets were sealed in a custom-built observation chamber and imaged 10 min after encapsulation using a confocal laser scanning microscope LSM 880 or LSM 800 (Carl Zeiss AG). The pinhole aperture was set to one Airy Unit and experiments were performed at room temperature. The images were acquired using a 20x objective (Plan-Apochromat 20x/0.8 M27, Carl Zeiss AG). Images were analyzed and processed with ImageJ (NIH, brightness and contrast adjusted).

Light-triggered proton release

To dynamically decrease the pH inside individual compartments, we co-encapsulated 40 mM NPE-caged sulfate (Santa Cruz Biotechnology), which undergoes photolysis upon illumination with light of the wavelength 405 nm and releases a proton. For the investigation of the detachment kinetics, 2 µM ssDNA and 1.5 µM tsDNA were mixed with 20 mM potassium phosphate buffer at pH 8 and 5 mM $MgCl_2$. The use of the buffer ensures the same starting conditions and delays the acidification, which facilitates the imaging and analysis of the tsDNA fluorescence. After encapsulation, a subset of droplets was illuminated with 20 % of the power of a 5 mW 405 nm laser diode while simultaneously recording the detachment of the Cy5-labelled tsDNA. The field of view, the laser intensity and all additional imaging conditions were kept the same.

Image analysis

The tsDNA fluorescence inside the droplet and at the droplet periphery was analysed with a custom-written ImageJ macro. Droplets were identified and assigned a circular region of interest from which the droplet radius r_0 was calculated. The intensity within the droplet center, I_{in}, was defined as the mean intensity within a circle of radius $r_{\text{in}} = 0.5r_0$. The intensity at the droplet periphery I_{peri} was quantified by measuring the maximum intensity

bioRxiv preprint doi: https://doi.org/10.1101/2020.12.12.422444; this version posted December 12, 2020. The copyright holder for this preprint (which was not certified by peer review) is the author/funder, who has granted bioRxiv a license to display the preprint in perpetuity. It is made available under aCC-BY 4.0 International license.

101 along a line orthogonal to the droplet circumference. This analysis was repeated 20 times
102 every 18° along the droplet circumference, and the mean value taken as I_{peri}. Following the
103 determination of the droplet intensities $\mathrm{I_{in}}$, they were plotted with Prism 8 (GraphPad) and
104 fitted using a sigmoidal function of the form: $I_{\mathrm{in}} = I_{\mathrm{min}} + (I_{\mathrm{min}} - I_{\mathrm{max}})/(1 + 10^{-\alpha(x_{\mathrm{turn}}-x)})$,
105 with α being the decay constant and x_{turn} the turning point of the fit.

106 Atomistic simulations of unlabeled ssDNA

107 To provide a realistic description of ssDNA dynamics both in the presence and in the ab-
108 sence of fluorescent dyes, we first performed a series of simulations for the dye-free ssDNA
109 using the Parmbsc1 flavour [27] of the standard Amber 99SB force field [28] with CUFIX non-
110 bonded corrections [29] and ion parameter corrections by Joung and Cheatham. [30] We also
111 used TIP3P as the water model in our simulations. [31] The simulations were initiated from
112 single-stranded helical structures built with Chimera (v. 1.14). [32] The starting structures
113 were solvated in TIP3P water in a dodecahedron box with an edge length of 9.0 nm, yielding
114 a system with approximately 50 000 atoms. Ion concentrations were set to 250 mM NaCl
115 and 10 mM $MgCl_2$ to mimic the experimental conditions.

116 Subsequent MD simulations were performed with GROMACS 2019.6. [33] Lennard-Jones
117 and short-range electrostatic interactions were calculated with a 1.0-nm cutoff, while long-
118 range electrostatics was treated using particle-mesh Ewald summation [34] with a 0.12-nm grid
119 spacing. Hydrogen bond lengths were constrained using the LINCS algorithm. [35] Velocity
120 rescaling [36] with a heat bath coupling constant of 1.0 ps was used to control the temperature
121 for solute and solvent separately. Center-of-mass correction was applied to solute and solvent
122 separately every 100 steps. Energy minimization was followed by a short equilibration for
123 1 ns in the NVT ensemble (T = 100 K) and with position restraints applied to the solute's
124 heavy atoms and a 1-fs integration time step. Next, the temperature was increased to T =
125 300 K, and the system was equilibrated for 5 ns (2-fs time step), while keeping the pressure at
126 1 atm using the Berendsen barostat [37] with a 1-ps coupling constant. The position restraints

bioRxiv preprint doi: https://doi.org/10.1101/2020.12.12.422444; this version posted December 12, 2020. The copyright holder for this preprint (which was not certified by peer review) is the author/funder, who has granted bioRxiv a license to display the preprint in perpetuity. It is made available under aCC-BY 4.0 International license.

127 were then slowly released during 20 ns of equilibration in the NPT ensemble (T = 300 K, p
128 = 1 atm, 2-fs time step) using the Parrinello-Rahman barostat.[38] This initial equilibration
129 step was followed by a total of 17 independent production runs, each being 5 μs long. The
130 first ∼1 μs of the trajectories were discarded to exclude the initial relaxation towards the
131 equilibrium state. Unless specified differently, all trajectory analyses were performed with
132 Python (v. 2.7 available at https://www.python.org/), VMD (v. 1.9.2)[39] and Chimera (v.
133 1.14).[32]

134 ssDNA simulations with fluorescent dyes covalently attached

135 Parameters and energy-minimized structures for common Alexa and Cy fluorescent dye fam-
136 ilies were derived from the AMBER-DYES library[40] that is compatible with most Amber
137 force fields. Alexa488, Cy3 (water-soluble) and C5 (water-soluble) dyes were attached to the
138 5' end of the ssDNA via a neutral lysine linker. To this end, the capping H5T atom of the
139 5' nucleotide was removed, and the C atom of the linker backbone was bonded with the O5'
140 atom of the 5' nucleotide. Since in the Amber formalism, the 5' and 3' nucleotides possess
141 non-integer charges (-0.3 e and -0.7 e, respectively; unlike the regular nucleotides that have
142 a charge of -1.0 e), the resulting dye-ssDNA construct had a slightly non-integer charge. To
143 account for this, the residual small charge was redistributed over the O5', C5', C4', C3', O4',
144 C1', and C2' atoms of the 5' nucleotide (sugar backbone).

145 To accommodate the larger dye-ssDNA, the size of the simulation box was increased to
146 12 nm, yielding a system with about 120 000 atoms. All subsequent simulations were done
147 under the same conditions as for the unlabeled ssDNA. For the dye-free simulations, multiple
148 6 µs production runs were performed and the first ∼1 µs were discarded as equilibration time.
149 A summary of the simulated systems is given in Table 1.

bioRxiv preprint doi: https://doi.org/10.1101/2020.12.12.422444; this version posted December 12, 2020. The copyright holder for this preprint (which was not certified by peer review) is the author/funder, who has granted bioRxiv a license to display the preprint in perpetuity. It is made available under aCC-BY 4.0 International license.

Table 1: Summary of dye-free and dye-labeled ssDNA simulations.

Force field	System	Duration
Parmbsc1 + TIP3P	no dye	17×5 μs
Parmbsc1 + TIP3P	Cy3	6×6 μs
Parmbsc1 + TIP3P	Cy5	6×6 μs
Parmbsc1 + TIP3P	Alexa 488	6×6 μs

150 ## Determination of the apparent dissociation constant

The equilibrium distribution of ssDNA and tsDNA molecules in a droplet can be described mathematically using a reaction-diffusion system of equations in which the binding sites (ssDNA attached to the droplet periphery), and hence also the binding and dissociation reactions, are localized in a narrow volumetric layer near the spherical droplet surface.[41,42] Briefly, if S_{tot} and T_{tot} are the total concentrations of ssDNA and tsDNA in the droplet, respectively, T_{eq} is the steady-state concentration of tsDNA in equilibrium, and K_{D} is the dissociation constant defining the ssDNA/tsDNA binding equilibrium, the ratio between the peripheral and inner intensity of tsDNA fluorescence can be expressed as:

$$\frac{I_{\text{peri}}}{I_{\text{in}}} = 1 + \frac{S_{\text{tot}}}{T_{\text{eq}} + K_{\text{D}}}. \tag{1}$$

Here, both I_{peri} and I_{in} are per-area intensities averaged over πr_{in}^2 and $2\pi r_0 \varepsilon$, respectively, where ε is the apparent thickness of the reaction layer (determined from confocal images as described in the Supplementary Text S1). The steady-state concentration T_{eq},

$$T_{\text{eq}} = \frac{1}{2}\Bigg[- \Big(3^{\varepsilon}/_{r_0} S_{\text{tot}} + K_{\text{D}} - T_{\text{tot}}\Big) + + \sqrt{(3^{\varepsilon}/_{r_0} S_{\text{tot}} + K_{\text{D}} - T_{\text{tot}})^2 + 4 T_{\text{tot}} K_{\text{D}}}\Bigg], \tag{2}$$

151 is obtained by simultaneously requiring that the ssDNA/tsDNA binding has attained equi-
152 librium and that the number of tsDNA molecules in the droplet is conserved. The apparent

bioRxiv preprint doi: https://doi.org/10.1101/2020.12.12.422444; this version posted December 12, 2020. The copyright holder for this preprint (which was not certified by peer review) is the author/funder, who has granted bioRxiv a license to display the preprint in perpetuity. It is made available under aCC-BY 4.0 International license.

K_D values presented in Figure 4 were determined using Eqs. 1 and 2, and the corresponding errors were calculated using basic error propagation rules and measured uncertainties of I_{peri}, I_{in}, r_0, and ε. A detailed mathematical description of the model, estimation of ε, and error analysis are given in the Supplementary Texts S1 and S2.

Radius of gyration distributions and estimations of confidence intervals

The gyration radii (R_g) of ssDNA were calculated using the `gmx gyrate` tool included in the GROMACS package. The probability distributions $p(R_g)$ shown in Figure 2 were then computed by binning the corresponding data sets and normalizing the histograms. Confidence intervals for $p(R_g)$ were estimated using bootstrap analysis.[43] To this end, we used the obtained distributions to bootstrap 10^6 new random R_g samples (each consisting of 10^5 data points) such that the newly generated data is distributed according to $p(R_g)$ and properly correlated with the autocorrelation time estimated from the original R_g trajectories.

Results

Fluorophore modification influences pH response

We set out to test the impact of fluorophores on the dynamics of DNA nanostructures. For this purpose, we employed a popular triple-stranded DNA motif (tsDNA)[4] as an example. Its reversible pH-responsive actuation works as follows: At basic pH, the Hoogsten-interactions which stabilize the triple-stranded configuration are weaker than at acidic pH. Therefore, an increase in pH leads to unwrapping of the third strand which previously stabilized the duplex. This, in turn, lowers the energy barrier for a strand displacement reaction with a single-stranded DNA (ssDNA), which was designed to be complementary to the hairpin loop of the tsDNA. Thus, a stable DNA duplex can form between the tsDNA and the

bioRxiv preprint doi: https://doi.org/10.1101/2020.12.12.422444; this version posted December 12, 2020. The copyright holder for this preprint (which was not certified by peer review) is the author/funder, who has granted bioRxiv a license to display the preprint in perpetuity. It is made available under aCC-BY 4.0 International license.

176 ssDNA (Figure 1**A**).[4] To monitor this process, we modified the ssDNA with a cholesterol-tag
177 and encapsulated it together with the tsDNA into water-in-oil droplets. Upon encapsula-
178 tion, the ssDNA self-assembled at the droplet periphery due to hydrophobic interactions
179 between the cholesterol-tag and the droplet-stabilizing surfactants.[11] Thereby, we obtained
180 an attachment handle, which reversibly recruits the tsDNA to the periphery at basic pH
181 (Figure 1**B**). In contrast to Förster Resonance Energy Transfer (FRET), which is commonly
182 employed to monitor the pH dynamics,[21] our system provides freedom regarding the choice
183 of fluorophores – which is absolutely necessary for us to study the impact of different fluo-
184 rophore combinations. We directly visualized tsDNA binding and investigated the impact
185 of fluorophore modifications on the pH dynamics. At the same time, this system provides a
186 strategic blueprint for the pH-sensitive recruitment of components to the membrane – an in-
187 teresting function in itself, in particular concerning the bottom-up construction of synthetic
188 cells.[44]

189 Confocal imaging revealed that attachment of the tsDNA to the compartment periphery
190 is shifted to higher pH values if the ssDNA carries a Cy3 compared to the unlabelled ssDNA
191 (Figure 1**C,D**). The images show the equilibrated state (Figure S1) and we confirmed that
192 the shift is not due to interactions of the Cy3 with the surfactant layer (Figure S2). We
193 quantified this effect by extracting the normalized intensity inside the droplets (I_{in}, periph-
194 ery excluded) from the confocal images (Figure 1**E**). Importantly, we could reproduce the
195 sigmoidal pH response curve that was reported for FRET-based detection.[45] The turning-
196 point of the pH-sensitive ssDNA-tsDNA binding curve for unlabelled ssDNA was around 5.80
197 $\pm$ 0.09, whereas it shifted significantly to 6.05 $\pm$ 0.04 for the Cy3-modified ssDNA (2.53σ).
198 Even at pH 8 not all tsDNA was bound to the droplet periphery for the Cy3-modified ssDNA.

199

200 While it is well known that the pH turning point can be shifted by changing the DNA
201 sequence,[45] it was not known that the same can be achieved by changing the fluorophore
202 modification alone. This striking observation can be explained by either of the two following

bioRxiv preprint doi: https://doi.org/10.1101/2020.12.12.422444; this version posted December 12, 2020. The copyright holder for this preprint (which was not certified by peer review) is the author/funder, who has granted bioRxiv a license to display the preprint in perpetuity. It is made available under aCC-BY 4.0 International license.

203 hypotheses as illustrated in Figure 1**F**: 1) A fluorophore modification on the ssDNA causes
204 overstabilization of the free ssDNA state by making its equilibrium ensemble more compact
205 and, therefore, less accessible for base paring. 2) The fluorophore modification destabilizes
206 the ssDNA-tsDNA complex, thereby raising the bound state in free energy (relative to the
207 unbound one). First, we tested Hypothesis 1 with all-atom molecular dynamics (MD) sim-
208 ulations, subsequently we examined Hypothesis 2 with experiments.

209 MD simulations reveal reduction of ssDNA accessibility by fluo-210 rophore modification

211 To test Hypothesis 1, we used all-atom MD simulations to probe the secondary structure
212 of the Cy3-labelled ssDNA (Figure 2**A**) and compared it to the unlabelled ssDNA. First
213 of all, the unlabelled ssDNA yielded a very broad probability density distributions for the
214 radius of gyration (Figure 2**B**), which is a direct measure of the DNA's compactness. The
215 distributions for the unlabelled ssDNA show a significant fraction of extended structures, in
216 which the DNA bases are accessible for complementary base pairing (see also representative
217 snapshots in Figure 2**C** and Video S1). On the contrary, the Cy3-labelled ssDNA (Figure
218 2**A**) yielded a distinctively different probability density distribution for the radius of gyration
219 (Figure 2**D**), which reflects a much lower propensity for extended conformations. The bases
220 of the Cy3-labelled ssDNA were found to be wrapped around the fluorophore, most likely due
221 to stacking interactions between the ssDNA bases and the aromatic groups of Cy3 (Video
222 S2). This entangled conformation renders the ssDNA less accessible for complementary
223 base pairing. An overstabilization of the unbound ssDNA means a lower free energy of
224 the ssDNA compared to the ssDNA-tsDNA complex. This would explain our experimental
225 observations in line with Hypothesis 1. Note that Cy5-labelled ssDNA favored similarly
226 compact conformations wrapped around the dye, which further indicates that the aromatic
227 groups of Cy dyes tend to interact with ssDNA base pairs (Figure S3, Video S3).

228 To test if weaker dye-ssDNA interactions would restore expanded conformations of the

bioRxiv preprint doi: https://doi.org/10.1101/2020.12.12.422444; this version posted December 12, 2020. The copyright holder for this preprint (which was not certified by peer review) is the author/funder, who has granted bioRxiv a license to display the preprint in perpetuity. It is made available under aCC-BY 4.0 International license.

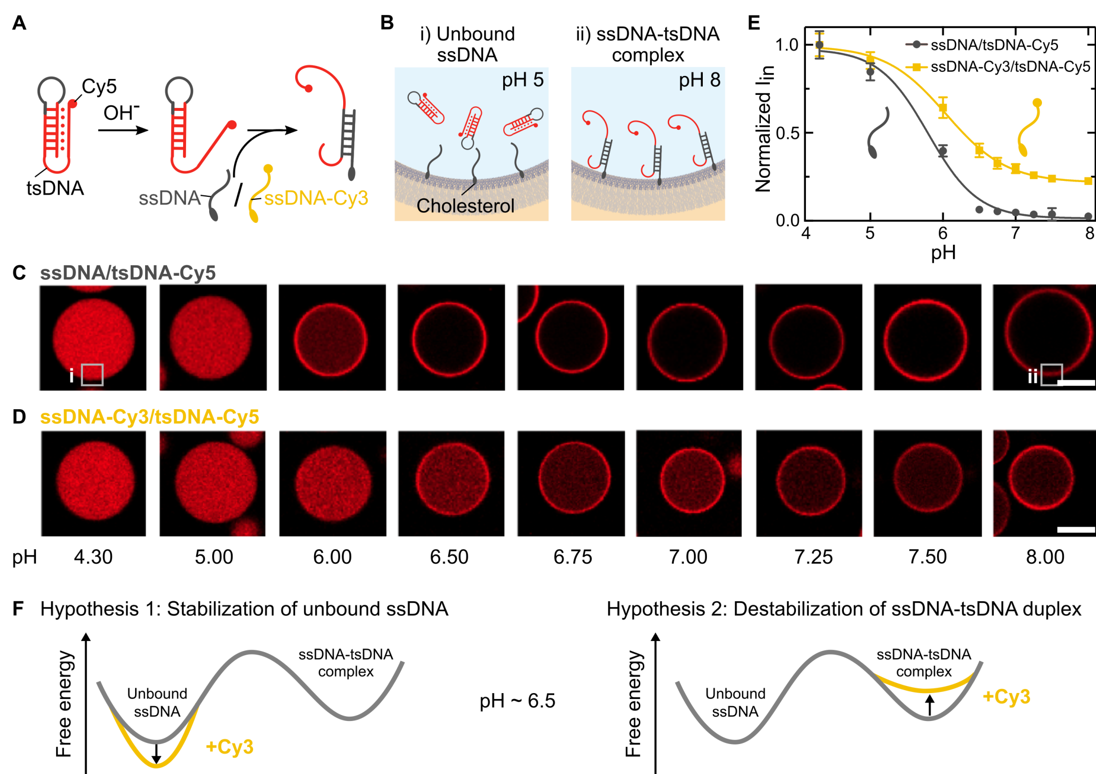

Figure 1: Fluorophore modification influences pH response. **A** Sketch of the pH responsive DNA motif. A Cy5-labeled triple-stranded DNA (tsDNA) opens up at basic pH, lowering the energy barrier for strand displacement and hence for complementary base pairing with a cholesterol-tagged single-stranded DNA (ssDNA). **B** This process can be monitored in water-in-oil droplets. The cholesterol-tagged ssDNA self-assembles at the droplet periphery, whereas cholesterol-free tsDNA remains homogeneously distributed within the droplet at acidic pH and attaches to the droplet periphery at higher pH values. **C, D** Representative confocal images of water-in-oil droplets containing Cy5-labeled tsDNA (red, $\lambda_{ex} = 647\,\text{nm}$) and unlabeled ssDNA (**D**) or Cy3-labeled ssDNA (**E**) at different pH values. Attachment of the tsDNA is shifted to higher pH values if the ssDNA is labelled with Cy3. Scale bars: 20 µm. **E** Normalized fluorescence intensity of the Cy5-labeled tsDNA inside the droplet (periphery excluded) at different pH values for unlabeled (gray) and Cy3-labeled ssDNA (yellow). Error bars correspond to the standard deviation of the intensities of n $\geq$ 9 droplets. Solid lines represent sigmoidal fits revealing a turning point at pH 5.80 $\pm$ 0.09 and 6.05 $\pm$ 0.04, respectively. **F** Free energy profile illustrating potential hypotheses for the altered behaviour of the Cy3-tagged ssDNA compared to the unlabelled ssDNA.

bioRxiv preprint doi: https://doi.org/10.1101/2020.12.12.422444; this version posted December 12, 2020. The copyright holder for this preprint (which was not certified by peer review) is the author/funder, who has granted bioRxiv a license to display the preprint in perpetuity. It is made available under aCC-BY 4.0 International license.

229 ssDNA in our simulations, we used an Alexa 488 dye. We selected an Alexa dye (Figure **2F**),
230 because its chemical structure is considerably different compared to Cy3, which may render
231 it less prone to base stacking interactions. Moreover, Alexa dyes are more hydrophilic due
232 to their two negative charges. We found that the mean radius of gyration for an Alexa488-
233 modified ssDNA laid between that of the unmodified and the Cy3-modified ssDNA (Figure
234 2**G**). The MD snapshots show that the fully extended conformation, where the bases are
235 accessible, was partially recovered (Figure 2**H**, Video S4), improving the accessibility of the
236 strand for complementary base pairing.

237 Taken together, our simulations suggest that a single fluorophore modification on ssDNA
238 can significantly change the DNA's conformation. The more compact conformation of dye-
239 labeled ssDNA effectively increases the free energy cost for expansion required for duplex
240 formation with tsDNA. Thus, our simulations support Hypothesis 1. Importantly, the ssDNA
241 sequence is random such that the observations can likely be generalized for a broad spectrum
242 of DNA sequences.

243 Dissociation kinetics show fluorophore dependence

244 As a next step, we investigated the duplex dissociation process to see if the fluorophore
245 modification affects the dissociation constant after duplex formation (Hypothesis 2). Since
246 all-atom MD simulations cannot describe this reaction due to the limited timescales, we
247 studied the detachment of the tsDNA from the compartment periphery experimentally. We
248 implemented an approach where we achieved light-triggered release of protons in individual
249 compartments – providing full spatio-temporal control over the acidification process. For
250 this purpose, we used NPE-caged-sulfate, which breaks up into a sulfate and a proton upon
251 photolysis.[46] To prove that NPE-caged sulfate can be used to decrease the pH inside the
252 droplets, we first encapsulated it together with the pH-sensitive dye pyranine at pH 8 and lo-
253 cally illuminated individual droplets with a 405 nm laser (Figure 3**A**). The pyranine emission
254 upon 488 nm excitation decreased, confirming the successful pH decrease inside the droplets

bioRxiv preprint doi: https://doi.org/10.1101/2020.12.12.422444; this version posted December 12, 2020. The copyright holder for this preprint (which was not certified by peer review) is the author/funder, who has granted bioRxiv a license to display the preprint in perpetuity. It is made available under aCC-BY 4.0 International license.

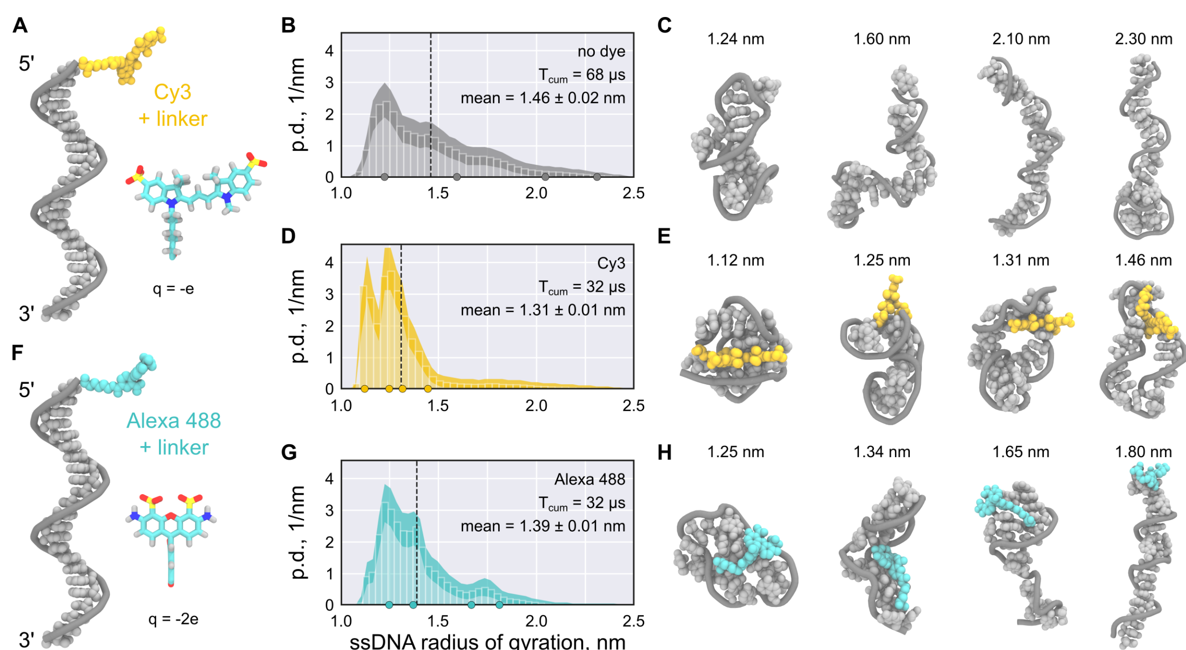

Figure 2: MD simulations suggest that fluorophore labeling can stabilize more compact ssDNA conformations. **A, F** Starting conformation of Cy3- (A, yellow) and Alexa488-labeled (F, turquoise) ssDNA (gray). The chemical structure of the fluorophore and its net charge are shown as an inset. **B, D, G** Probability density (p.d.) distributions of the gyration radius of ssDNA without dye (B), labeled with Cy3 (D), and labeled with Alexa488 (G). The shaded areas indicate the 95% confidence intervals estimated using bootstrapping (see Methods). The black dashed lines indicate the means of the distributions, T_{cum} the cumulative simulation time. **C, E, H** Representative structure snapshots of the unlabelled ssDNA (C), the Cy3-ssDNA (E) and the Alexa488-ssDNA (H). Positions of the selected snapshots within the corresponding distributions are marked with dots in the probability density distributions.

bioRxiv preprint doi: https://doi.org/10.1101/2020.12.12.422444; this version posted December 12, 2020. The copyright holder for this preprint (which was not certified by peer review) is the author/funder, who has granted bioRxiv a license to display the preprint in perpetuity. It is made available under aCC-BY 4.0 International license.

255 from initially pH 8 to under pH 5. The buffer kept the pH constant until its capacity is
256 exceeded after approximately 20 s. Then, the pH decreased until most of the NPE-caged
257 sulfate underwent photolysis and hence the pH approached a constant value after ∼50 s. We
258 used this dynamic light-mediated acidification mechanism to detach the tsDNA from the
259 droplet periphery. At t=0 s, the tsDNA was bound to the ssDNA at the droplet periphery
260 (Figure 3**B**) and completely detached within 50 s of illumination. Upon detachment, the
261 triplex conformation of the tsDNA was restored. In order to assess the detachment kinet-
262 ics, we monitored the normalized tsDNA-Cy5 intensity for unmodified, Cy3-modified and
263 Alexa488-modified ssDNA inside the droplet over time (Figure 3**C**).

264 Following proton-release, the tsDNA detached from the ssDNA for all tested fluorophore
265 modifications (Video S5).

266 The decay times $t_d = 1/\alpha$ of the sigmoidal fits were comparable for all three fluorophore
267 modifications, indicating similar detachment kinetics. However, detachment (i.e. duplex
268 dissociation) occurred at different time points, hence at different pH values – again pointing
269 towards an altered binding equilibrium. Detachment from the unlabelled ssDNA happened
270 earlier (i.e. at higher pH) indicating that a fluorophore label is stabilizing the ssDNA-tsDNA
271 complex.

272 Taken together, the results obtained so far suggest that fluorophore modifications, in par-
273 ticular Cy-dyes, stabilize not only the unbound ssDNA (Hypothesis 1) but also the ssDNA-
274 tsDNA duplex as illustrated in the free energy profile in Figure 3**D**. However, the stabiliza-
275 tion of compact ssDNA conformations is likely stronger, which explains the observed shift
276 of the pH switching point. This is effectively increasing the energy barrier for the dynamic
277 switching of fluorophore-labelled DNA.

bioRxiv preprint doi: https://doi.org/10.1101/2020.12.12.422444; this version posted December 12, 2020. The copyright holder for this preprint (which was not certified by peer review) is the author/funder, who has granted bioRxiv a license to display the preprint in perpetuity. It is made available under aCC-BY 4.0 International license.

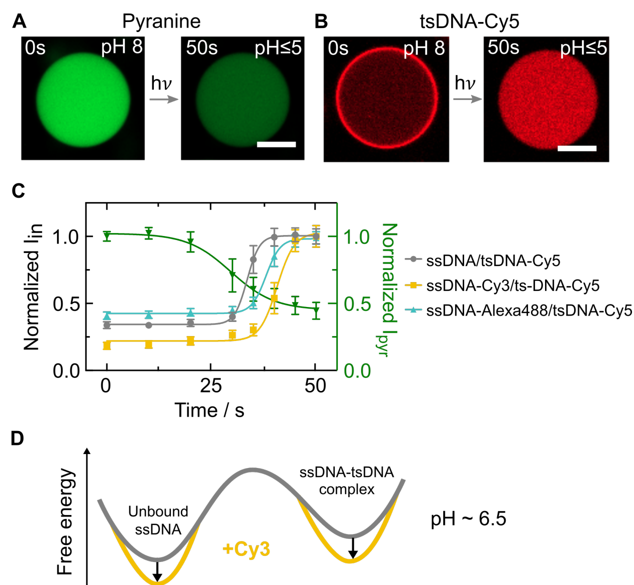

Figure 3: Light-mediated acidification of water-in-oil droplets reveals fluorophore-dependent duplex dissociation kinetics. **A** Confocal images of the pH-sensitive dye pyranine (50 µM, $\lambda_{ex} = 488$ nm, not coupled to DNA) encapsulated into water-in-oil droplets at pH 8. Light-triggered uncaging of NPE-caged sulfate ($\lambda_{ex} = 405$ nm) leads to proton release causing a rapid pH drop from 8 to under 5 within 50 s. The pH drop can be monitored as a decrease in pyranine fluorescence. **B** Representative confocal images of Cy5-labeled tsDNA ($\lambda_{ex} = 647$ nm) encapsulated together with cholesterol-tagged ssDNA into water-in-oil droplets at pH 8. During acidification, the tsDNA detaches from the droplet periphery as the triplex state is energetically favoured. Scale bars: 20 µm. **C** Normalized fluorescence intensity of the tsDNA inside the droplet (periphery excluded) over time for unlabeled, Cy3-labeled and Alexa488-labeled ssDNA as well as pyranine (right axis). Error bars correspond to the standard deviation of the intensities of n $\geq$ 23 droplets for the DNA experiments and n = 6 droplets for pyranine experiments. Solid lines represent sigmoidal fits with turning points at 33.5 s $\pm$ 0.1 s (unmodified ssDNA), 40.7 s $\pm$ 0.5 s (ssDNA-Cy3) and 38.0 s $\pm$ 0.3 s (ssDNA-Alexa488). Note that the decay times $t_d = 1/\alpha$ are similar for all fluorophores 3 45s $\pm$ 0.24 s (unmodified ssDNA), 4.76 s $\pm$ 1.13 s (ssDNA-Cy3) and 4.00 s $\pm$ 0.48 s (ssDNA-Alexa488). **D** Free energy profile illustrating our conclusion that both equilibrium states are stabilized by the presence of a dye on the ssDNA.

bioRxiv preprint doi: https://doi.org/10.1101/2020.12.12.422444; this version posted December 12, 2020. The copyright holder for this preprint (which was not certified by peer review) is the author/funder, who has granted bioRxiv a license to display the preprint in perpetuity. It is made available under aCC-BY 4.0 International license.

Reaction-diffusion modelling reveals impact of fluorophores on apparent dissociation constant

Finally, having shown that a fluorophore modification on the ssDNA has a significant influence on the pH switching point, we now additionally tested the impact of fluorophore modifications on tsDNA. For this purpose, we investigated twelve different fluorophore combinations on ssDNA and tsDNA. To quantitatively compare the impact of different fluorophores, we developed an analytical model to derive the apparent dissociation equilibrium constant $K_{\mathrm{D}} = k_{\mathrm{off}}/k_{\mathrm{on}}$ at a fixed pH for each individual fluorophore combination. For this purpose, we derived a reaction-diffusion model for spherical compartments (Text S2). It allowed us to determine the apparent dissociation constant K_{D} by extracting the droplet radius, the peripheral and the inner intensity of the tsDNA from confocal images with known total concentrations of DNA. We tested combinations of five different fluorophores, namely Cy3, Cy5, Alexa488, Atto488 and Atto647 as well as unlabeled ssDNA on the apparent K_{D} (Figure 4). Note that the use of an unlabelled tsDNA was not possible because it would inhibit the monitoring with confocal microscopy.

Remarkably, K_{D} varied dramatically for the different combinations. Most striking was the fact that binding is almost fully inhibited for certain fluorophore combinations, like ssDNA/tsDNA-Atto647, ssDNA-Cy5/tsDNA-Atto488 and ssDNA-Alexa488/tsDNA-Atto647 with $K_{\mathrm{D}} \gg 1$. On the other hand combinations like ssDNA-Cy3/ts-DNACy5, ssDNA/tsDNA-Cy3 and ssDNA/tsDNA-Cy5 bound very efficiently as expected at pH 8. As a general trend, we deduce that Cy-dyes on the tsDNA seemed to lead to a lower apparent K_{D} compared to Atto-dyes. Furthermore, it is surprising that the permutation of two Cy-dyes on ssDNA and tsDNA lead to a different apparent K_{D}. While ssDNA-Cy3/tsDNA-Cy5 attached very efficiently, we obtained intermediate K_{D}'s for ssDNA-Cy5/tsDNA-Cy3. Confirming our observations, the permutation of the tsDNA fluorophore influenced the pH hysteresis (Figure S4) and the dynamic detachment in experiments using NPE-caged sulfate (Figure S5).

Taking all these observations into account, we propose that not only a fluorophore mod-

bioRxiv preprint doi: https://doi.org/10.1101/2020.12.12.422444; this version posted December 12, 2020. The copyright holder for this preprint (which was not certified by peer review) is the author/funder, who has granted bioRxiv a license to display the preprint in perpetuity. It is made available under aCC-BY 4.0 International license.

305 ification on the ssDNA but also on the tsDNA affects the dynamics of pH-responsive DNA
306 nanostructures up to a point that binding is inhibited. The choice of fluorescent dyes can
307 thus be exploited to shape the energy landscape for dynamic DNA nanostructures and to
308 shift the equilibrium towards the bound or the unbound state.

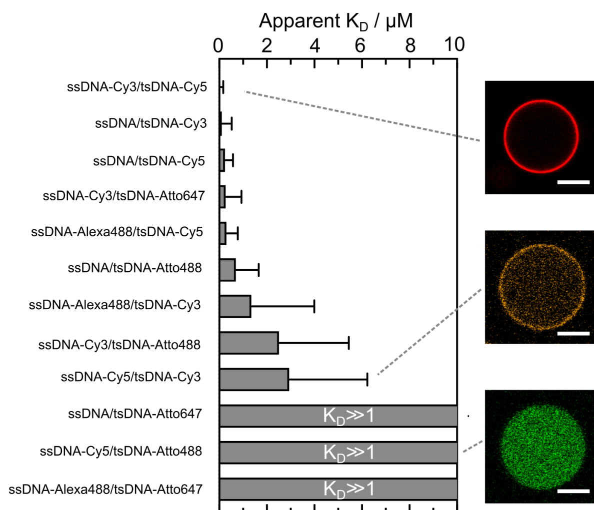

Figure 4: Histogram depicting the apparent dissociation constants K_D for 12 different ssDNA/tsDNA combinations at pH 8 with variable fluorophore modifications including Alexa488 ($\lambda_{ex} = 488$ nm), Atto488 ($\lambda_{ex} = 488$ nm), Cy3 ($\lambda_{ex} = 561$ nm), Cy5 ($\lambda_{ex} = 647$ nm) and Atto647 ($\lambda_{ex} = 647$ nm). Error bars correspond to the standard deviation of n = 11-73 evaluated droplets. Confocal images of three fluorophore combinations depicting strong (ssDNA-Cy3/tsDNA-Cy5), intermediate (ssDNA-Cy5/tsDNA-Cy3) and almost no binding to the droplet periphery (ssDNA-Cy5/tsDNA-Atto488). The apparent K_D is strongly influenced by fluorophore modifications on ssDNA and tsDNA up to the point of almost full inhibition of binding, which results in $K_D \gg 1$.

309 # Discussion

310 One of the most exciting tasks in the field of DNA nanotechnology is the construction of
311 dynamic molecular devices that can perform mechanical motion upon stimulation. The
312 foundation for this work is an experimental readout, which is suitable to track dynamic
313 reconfiguration in space and time. Fluorescence microscopy techniques, such as superresolu-
314 tion imaging or FRET, are ideally suited for *in situ* measurements on active DNA origami

bioRxiv preprint doi: https://doi.org/10.1101/2020.12.12.422444; this version posted December 12, 2020. The copyright holder for this preprint (which was not certified by peer review) is the author/funder, who has granted bioRxiv a license to display the preprint in perpetuity. It is made available under aCC-BY 4.0 International license.

315 structures. The fluorophore is normally selected to match the optical setup rather than
316 the DNA nanostructure itself and exchanged as required by the experiment. Here, we de-
317 termined why the exchange of fluorophores on dynamic DNA nanostructures can lead to a
318 considerably different experimental outcome. We used a popular pH-sensitive DNA motif
319 combined with a strand displacement reaction as an example to show that the fluorophore
320 alone can alter and even completely inhibit the dynamics. Strand-displacement is one of the
321 best understood and highly specific methods of actuating large DNA devices, but still has a
322 large potential for improvement with respect to kinetics. Addressing this challenge, we find
323 that fluorophores tend to stabilize the equilibrium states of the system with different effects
324 on its dynamics, whereby Cy-dyes are more prone to inhibit dynamics compared to Atto-
325 dyes. Beyond fluorophore labelling, DNA nanotechnology uses a myriad of other chemical
326 modifications on the DNA, form reactive amine or thiol groups, hydrophobic tags, spacers,
327 photocleavable groups or modifications for click chemistry.[47] We anticipate that our obser-
328 vations are not limited to dye molecules – these other chemical modification would very likely
329 have similar effects. It is thus generally possible to shape the energy landscape for dynamic
330 reconfiguration as well as the equilibrium configuration without changing the DNA sequence.
331

332 Our results are directly relevant for various applications that capitalize on dynamic DNA
333 systems, from bottom-up synthetic biology to biosensing and the the increasingly popular su-
334 perresolution technique DNA-PAINT.[23] Without doubt, the possibility to precisely shape
335 energy landscapes for dynamic DNA nanostructures will lead to metastable DNA nanos-
336 tructures and fully reversible DNA devices with unprecedented complexity – mimicking the
337 intricate workings of natural nanomachines.

bioRxiv preprint doi: https://doi.org/10.1101/2020.12.12.422444; this version posted December 12, 2020. The copyright holder for this preprint (which was not certified by peer review) is the author/funder, who has granted bioRxiv a license to display the preprint in perpetuity. It is made available under aCC-BY 4.0 International license.

Acknowledgement

The authors acknowledge Tobias Abele for help with the analysis of the droplet's peripheral intensity. K.G. acknowledges funding from the Deutsche Forschungsgemeinschaft (DFG, German Research Foundation) under Germany's Excellence Strategy via the Excellence Cluster 3D Matter Made to Order (EXC-2082/1 – 390761711). The work was further supported by the DFG via the principal investigator grant IG 109/1-1 awarded to M.I. Computational resources were provided by the Max Planck Computing and Data Facility and the Leibniz Supercomputing Centre (Garching, Germany). K.J. thanks the Carl Zeiss Foundation for financial support. All authors acknowledge the Max Planck Society for its general support.

Supporting Information Available

Competing interests

The authors declare no competing interests.

bioRxiv preprint doi: https://doi.org/10.1101/2020.12.12.422444; this version posted December 12, 2020. The copyright holder for this preprint (which was not certified by peer review) is the author/funder, who has granted bioRxiv a license to display the preprint in perpetuity. It is made available under aCC-BY 4.0 International license.

350 # References

351 (1) Ramezani, H.; Dietz, H. Building machines with DNA molecules. *Nature Reviews Ge-*
352 *netics* **2020**, *21*, 5–26.

353 (2) Nickels, P. C.; Wünsch, B.; Holzmeister, P.; Bae, W.; Kneer, L. M.; Grohmann, D.; Tin-
354 nefeld, P.; Liedl, T. Molecular force spectroscopy with a DNA origami–based nanoscopic
355 force clamp. *Science* **2016**, *354*, 305–307.

356 (3) Dutta, P. K.; Zhang, Y.; Blanchard, A. T.; Ge, C.; Rushdi, M.; Weiss, K.; Zhu, C.;
357 Ke, Y.; Salaita, K. Programmable Multivalent DNA-Origami Tension Probes for Re-
358 porting Cellular Traction Forces. *Nano Letters* **2018**, *18*, 4803–4811.

359 (4) Green, L. N.; Amodio, A.; Subramanian, H. K. K.; Ricci, F.; Franco, E. pH-Driven
360 Reversible Self-Assembly of Micron-Scale DNA Scaffolds. *Nano Letters* **2017**, *17*, 7283–
361 7288.

362 (5) Ausländer, S.; Ausländer, D.; Fussenegger, M. Synthetic Biology—The Synthesis of
363 Biology. *Angewandte Chemie - International Edition* **2017**, *56*, 6396–6419.

364 (6) Jiang, Q.; Song, C.; Nangreave, J.; Liu, X.; Lin, L.; Qiu, D.; Wang, Z.-G.; Zou, G.;
365 Liang, X.; Yan, H.; Ding, B. DNA Origami as a Carrier for Circumvention of Drug
366 Resistance. *Journal of the American Chemical Society* **2012**, *134*, 13396–13403.

367 (7) Wang, C.; Vázquez-González, M.; Fadeev, M.; Sohn, Y. S.; Nechushtai, R.; Willner, I.
368 Thermoplasmonic-Triggered Release of Loads from DNA-Modified Hydrogel Microcap-
369 sules Functionalized with Au Nanoparticles or Au Nanorods. *Small* **2020**, *16*, 2000880.

370 (8) Marras, A. E.; Zhou, L.; Su, H.-J.; Castro, C. E. Programmable motion of DNA origami
371 mechanisms. *Proceedings of the National Academy of Sciences* **2015**, *112*, 713–718.

372 (9) Simmel, F. C.; Schulman, R. Self-organizing materials built with DNA. *MRS Bulletin*
373 **2017**, *42*, 913–919.

bioRxiv preprint doi: https://doi.org/10.1101/2020.12.12.422444; this version posted December 12, 2020. The copyright holder for this preprint (which was not certified by peer review) is the author/funder, who has granted bioRxiv a license to display the preprint in perpetuity. It is made available under aCC-BY 4.0 International license.

374 (10) Franquelim, H. G.; Dietz, H.; Schwille, P. Reversible membrane deformations by
375 straight DNA origami filaments. *Soft Matter* **2020**,

376 (11) Jahnke, K.; Weiss, M.; Frey, C.; Antona, S.; Janiesch, J.-W.; Platzman, I.; Göpfrich, K.;
377 Spatz, J. P. Programmable Functionalization of Surfactant-Stabilized Microfluidic
378 Droplets via DNA-Tags. *Advanced Functional Materials* **2019**, *29*, 1808647.

379 (12) Jahnke, K.; Weiss, M.; Weber, C.; Platzman, I.; Göpfrich, K.; Spatz, J. P. Engineering
380 Light-Responsive Contractile Actomyosin Networks with DNA Nanotechnology. *Ad-*
381 *vanced Biosystems* **2020**, 2000102.

382 (13) Zhang, D. Y.; Winfree, E. Control of DNA Strand Displacement Kinetics Using Toehold
383 Exchange. *Journal of the American Chemical Society* **2009**, *131*, 17303–17314.

384 (14) Irmisch, P.; Ouldridge, T. E.; Seidel, R. Modeling DNA-Strand Displacement Reactions
385 in the Presence of Base-Pair Mismatches. *Journal of the American Chemical Society*
386 **2020**, *142*, 11451–11463.

387 (15) Kopperger, E.; List, J.; Madhira, S.; Rothfischer, F.; Lamb, D. C.; Simmel, F. C. A
388 self-assembled nanoscale robotic arm controlled by electric fields. *Science* **2018**, *359*,
389 296–301.

390 (16) Hernández-Ainsa, S.; Ricci, M.; Hilton, L.; Aviñó, A.; Eritja, R.; Keyser, U. F. Control-
391 ling the Reversible Assembly of Liposomes through a Multistimuli Responsive Anchored
392 DNA. *Nano Letters* **2016**, *16*, 4462–4466.

393 (17) Turek, V. A.; Chikkaraddy, R.; Cormier, S.; Stockham, B.; Ding, T.; Keyser, U. F.;
394 Baumberg, J. J. Thermo-Responsive Actuation of a DNA Origami Flexor. *Advanced*
395 *Functional Materials* **2018**, *28*, 1706410.

396 (18) Wang, J.; Yue, L.; Wang, S.; Willner, I. Triggered Reversible Reconfiguration of

bioRxiv preprint doi: https://doi.org/10.1101/2020.12.12.422444; this version posted December 12, 2020. The copyright holder for this preprint (which was not certified by peer review) is the author/funder, who has granted bioRxiv a license to display the preprint in perpetuity. It is made available under aCC-BY 4.0 International license.

397 G-Quadruplex-Bridged "Domino"-Type Origami Dimers: Application of the Systems
398 for Programmed Catalysis. *ACS Nano* **2018**, *12*, 12324–12336.

399 (19) Chen, Y.; Lee, S.-H.; Mao, C. A DNA Nanomachine Based on a Duplex–Triplex Tran-
400 sition. *Angewandte Chemie* **2004**, *116*, 5449–5452.

401 (20) Yang, M.; Zhang, X.; Liu, H.; Kang, H.; Zhu, Z.; Yang, W.; Tan, W. Stable DNA
402 Nanomachine Based on Duplex–Triplex Transition for Ratiometric Imaging Instanta-
403 neous pH Changes in Living Cells. *Analytical Chemistry* **2015**, *87*, 5854–5859.

404 (21) Patino, T.; Porchetta, A.; Jannasch, A.; Lladó, A.; Stumpp, T.; Schäffer, E.; Ricci, F.;
405 Sánchez, S. Self-Sensing Enzyme-Powered Micromotors Equipped with pH-Responsive
406 DNA Nanoswitches. *Nano Letters* **2019**, *19*, 3440–3447.

407 (22) Weiss, L. E.; Ezra, Y. S.; Goldberg, S.; Ferdman, B.; Adir, O.; Schroeder, A.;
408 Alalouf, O.; Shechtman, Y. Three-dimensional localization microscopy in live flowing
409 cells. *Nature Nanotechnology* **2020**, *15*, 500–506.

410 (23) Cnossen, J.; Hinsdale, T.; Thorsen, R. Ø.; Siemons, M.; Schueder, F.; Jungmann, R.;
411 Smith, C. S.; Rieger, B.; Stallinga, S. Localization microscopy at doubled precision with
412 patterned illumination. *Nature Methods* **2020**, *17*, 59–63.

413 (24) Moreira, B. G.; You, Y.; Owczarzy, R. Cy3 and Cy5 dyes attached to oligonucleotide
414 terminus stabilize DNA duplexes: Predictive thermodynamic model. *Biophysical Chem-*
415 *istry* **2015**, *198*, 36–44.

416 (25) Kaji, T.; Ito, S.; Iwai, S.; Miyasaka, H. Nanosecond to Submillisecond Dynamics in Dye-
417 Labeled Single-Stranded DNA, As Revealed by Ensemble Measurements and Photon
418 Statistics at Single-Molecule Level. *The Journal of Physical Chemistry B* **2009**, *113*,
419 13917–13925.

bioRxiv preprint doi: https://doi.org/10.1101/2020.12.12.422444; this version posted December 12, 2020. The copyright holder for this preprint (which was not certified by peer review) is the author/funder, who has granted bioRxiv a license to display the preprint in perpetuity. It is made available under aCC-BY 4.0 International license.

420 (26) Göpfrich, K.; Haller, B.; Staufer, O.; Dreher, Y.; Mersdorf, U.; Platzman, I.; Spatz, J. P.
421 One-Pot Assembly of Complex Giant Unilamellar Vesicle-Based Synthetic Cells. *ACS*
422 *Synthetic Biology* **2019**, *8*, 937–947.

423 (27) Ivani, I. et al. Parmbsc1: A refined force field for DNA simulations. *Nature Methods*
424 **2015**, *13*, 55–58.

425 (28) Hornak, V.; Abel, R.; Okur, A.; Strockbine, B.; Roitberg, A.; Simmerling, C. Com-
426 parison of multiple Amber force fields and development of improved protein backbone
427 parameters. *Proteins: Structure, Function, and Bioinformatics* **2006**, *65*, 712–725.

428 (29) Yoo, J.; Aksimentiev, A. New tricks for old dogs: Improving the accuracy of biomolec-
429 ular force fields by pair-specific corrections to non-bonded interactions. *Physical Chem-*
430 *istry Chemical Physics* **2018**, *20*, 8432–8449.

431 (30) Joung, I. S.; Cheatham, T. E. Determination of Alkali and Halide Monovalent Ion
432 Parameters for Use in Explicitly Solvated Biomolecular Simulations. *The Journal of*
433 *Physical Chemistry B* **2008**, *112*, 9020–9041.

434 (31) Chatterjee, S.; Debenedetti, P. G.; Stillinger, F. H.; Lynden-Bell, R. M. A computa-
435 tional investigation of thermodynamics, structure, dynamics and solvation behavior in
436 modified water models. *The Journal of Chemical Physics* **2008**, *128*, 124511.

437 (32) Pettersen, E. F.; Goddard, T. D.; Huang, C. C.; Couch, G. S.; Greenblatt, D. M.;
438 Meng, E. C.; Ferrin, T. E. UCSF Chimera - A visualization system for exploratory
439 research and analysis. *Journal of Computational Chemistry* **2004**, *25*, 1605–1612.

440 (33) Abraham, M.; van der Spoel, D.; Lindahl, E.; Hess, B. GROMACS User Manual version
441 2019. 2019; http://www.gromacs.org.

442 (34) Essmann, U.; Perera, L.; Berkowitz, M. L.; Darden, T.; Lee, H.; Pedersen, L. G. A

bioRxiv preprint doi: https://doi.org/10.1101/2020.12.12.422444; this version posted December 12, 2020. The copyright holder for this preprint (which was not certified by peer review) is the author/funder, who has granted bioRxiv a license to display the preprint in perpetuity. It is made available under aCC-BY 4.0 International license.

443 smooth particle mesh Ewald method. *The Journal of Chemical Physics* **1995**, *103*,
444 8577–8593.

445 (35) Hess, B.; Kutzner, C.; van der Spoel, D.; Lindahl, E. GROMACS 4: Algorithms for
446 Highly Efficient, Load-Balanced, and Scalable Molecular Simulation. *Journal of Chem-*
447 *ical Theory and Computation* **2008**, *4*, 435–47.

448 (36) Bussi, G.; Donadio, D.; Parrinello, M. Canonical sampling through velocity rescaling.
449 *The Journal of Chemical Physics* **2007**, *126*, 014101.

450 (37) Berendsen, H. J. C.; Postma, J. P. M.; van Gunsteren, W. F.; DiNola, A.; Haak, J. R.
451 Molecular dynamics with coupling to an external bath. *The Journal of Chemical Physics*
452 **1984**, *81*, 3684–3690.

453 (38) Parrinello, M.; Rahman, A. Polymorphic transitions in single crystals: A new molecular
454 dynamics method. *Journal of Applied Physics* **1981**, *52*, 7182–7190.

455 (39) Humphrey, W.; Dalke, A.; Schulten, K. VMD: Visual molecular dynamics. *Journal of*
456 *Molecular Graphics* **1996**, *14*, 33–38.

457 (40) Graen, T.; Hoefling, M.; Grubmüller, H. AMBER-DYES: Characterization of Charge
458 Fluctuations and Force Field Parameterization of Fluorescent Dyes for Molecular Dy-
459 namics Simulations. *Journal of Chemical Theory and Computation* **2014**, *10*, 5505–
460 5512.

461 (41) Hale, J.; Raugel, G. *Mathematics in Science and Engineering*; 1992; pp 63–97.

462 (42) Fibich, G.; Gannot, I.; Hammer, A.; Schochet, S. Chemical Kinetics on Surfaces: A
463 Singular Limit of a Reaction-Diffusion System. *SIAM Journal on Mathematical Analysis*
464 **2007**, *38*, 1371–1388.

465 (43) Hub, J. S.; De Groot, B. L.; van der Spoel, D. g_wham - a free Weighted Histogram

bioRxiv preprint doi: https://doi.org/10.1101/2020.12.12.422444; this version posted December 12, 2020. The copyright holder for this preprint (which was not certified by peer review) is the author/funder, who has granted bioRxiv a license to display the preprint in perpetuity. It is made available under aCC-BY 4.0 International license.

466 Analysis implementation including robust error and autocorrelation estimates. *Journal*
467 *of Chemical Theory and Computation* **2010**, *6*, 3713–3720.

468 (44) Czogalla, A.; Franquelim, H. G.; Schwille, P. DNA nanostructures on membranes as
469 tools for synthetic biology. *Biophysical Journal* **2016**, *110*, 1698–707.

470 (45) Idili, A.; Vallée-Bélisle, A.; Ricci, F. Programmable pH-Triggered DNA Nanoswitches.
471 *Journal of the American Chemical Society* **2014**, *136*, 5836–5839.

472 (46) Abbruzzetti, S.; Sottini, S.; Viappiani, C.; Corrie, J. E. T. Kinetics of Proton Release
473 after Flash Photolysis of 1-(2-Nitrophenyl)ethyl Sulfate (Caged Sulfate) in Aqueous
474 Solution. *Journal of the American Chemical Society* **2005**, *127*, 9865–9874.

475 (47) Madsen, M.; Gothelf, K. V. Chemistries for DNA Nanotechnology. *Chemical Reviews*
476 **2019**, *119*, 6384–6458.